



# Metasurface-based bijective illumination collection imaging provides high-resolution tomography in three dimensions

Masoud Pahlevaninezhad<sup>1,2,3</sup>, Yao-Wei Huang<sup>4,6</sup>, Majid Pahlevani<sup>2</sup>, Brett Bouma<sup>1,5</sup>, Melissa J. Suter<sup>1</sup>, Federico Capasso<sup>4</sup> and Hamid Pahlevaninezhad<sup>1,4</sup>

**Microscopic imaging in three dimensions enables numerous biological and clinical applications. However, high-resolution optical imaging preserved in a relatively large depth range is hampered by the rapid spread of tightly confined light due to diffraction. Here, we show that a particular disposition of light illumination and collection paths liberates optical imaging from the restrictions imposed by diffraction. This arrangement, realized by metasurfaces, decouples lateral resolution from the depth of focus by establishing a one-to-one correspondence (bijection) along a focal line between the incident and collected light. Implementing this approach in optical coherence tomography, we demonstrate tissue imaging at a wavelength of 1.3  $\mu\text{m}$  with  $\sim 3.2 \mu\text{m}$  lateral resolution, maintained nearly intact over a 1.25 mm depth of focus, with no additional acquisition or computational burden. This method, termed bijective illumination collection imaging, is general and might be adapted across various existing imaging modalities.**

High-resolution imaging of tissue microstructures is instrumental to biology and enables numerous clinical applications. Optical microscopy using tightly focused light, however, cannot be maintained in a relatively large depth range due to the rapid spreading of light dictated by diffraction. Imaging modalities such as confocal<sup>1</sup> and two-photon<sup>2</sup> microscopies achieve high-resolution imaging only for a narrow region around the focal point. Thus, additional scanning mechanisms are necessary to axially translate the focal point with respect to the target for depth-resolved imaging<sup>3</sup>. This impedes rapid imaging and the imaging depth, often limited to a few hundred micrometres<sup>4</sup>, which is inadequate for many applications.

Using coherence gating, optical coherence tomography (OCT) captures real-time depth-resolved images of structures millimetres deep into the scattering tissue<sup>5–9</sup>. Although this addresses axial resolution, OCT is still challenged by the competing lateral resolution and depth of focus due to diffraction that impedes high-resolution imaging in three dimensions in a large depth range<sup>10–12</sup>.

The central question is how the light intensity should be distributed to obtain high-resolution imaging in three dimensions in a large depth range. Focusing light on a single-depth point, which is widely used in the existing imaging systems, yields arbitrary primacy to that point, which is inconsistent with the goal of depth imaging. Alternatively, more equitable distribution of the optical intensity along the axial direction inevitably compromises the lateral resolution due to diffraction.

Here, we present a concept termed bijective illumination collection imaging (BICI) to accomplish high-resolution imaging in three dimensions in a relatively large depth range. This is achieved through a particular disposition of the illumination and collection paths that

allows a one-to-one spatial correspondence (bijection) between the illumination and collection light defined exclusively along a focal line. The impact on imaging is demonstrated by applying BICI to overcome the limitations of high-resolution OCT. Metasurfaces<sup>13–17</sup> with the ability to impart tailored phases are used to realize the illumination and collection paths required for the implementation of BICI. We report a lateral resolution of  $\sim 3.2 \mu\text{m}$  that is maintained nearly intact over an imaging depth of 1.25 mm, giving an imaging depth of focus that is around 12-fold larger compared with that obtained using an ideal Gaussian beam with the same lateral resolution. The imaging of swine tracheobronchial tissue specimens indicates the potential of BICI for high-resolution imaging preserved in a large depth range.

## Concept

The boundaries of lateral resolution and depth of focus are coupled with diffraction (depth of focus  $\approx \lambda/\text{NA}^2$ , where  $\lambda$  is the wavelength and NA is the numerical aperture). There exists a class of so-called diffraction-free<sup>18–23</sup> solutions to the Helmholtz equation. However, these modes in their exact mathematical forms have spatially unbounded profiles (plane waves are a trivial example) and give rise to side lobes that carry a substantial portion of the optical power (even in their physical realizations limited by a finite aperture). When used for imaging, the out-of-focus scattering from the side lobes compromises the imaging resolution and sensitivity.

Revisiting the lateral resolution and depth of focus in the context of the imaging point spread function (PSF) provides opportunities to evade the restrictions imposed by diffraction. The PSF at any point is the product of the probabilities of photons illuminating ( $P_{\text{ill}}$ ) and collected from ( $P_{\text{coll}}$ ) that point:  $\text{PSF} = P_{\text{ill}} \times P_{\text{coll}}$  (refs. <sup>24,25</sup>).

<sup>1</sup>Harvard Medical School and Massachusetts General Hospital, Boston, MA, USA. <sup>2</sup>Department of Electrical and Computer Engineering, Queen's University, Kingston, Ontario, Canada. <sup>3</sup>Department of Mechanical and Materials Engineering, Queen's University, Kingston, Ontario, Canada. <sup>4</sup>Harvard John A. Paulson School of Engineering and Applied Sciences, Harvard University, Cambridge, MA, USA. <sup>5</sup>Harvard-MIT Health Science and Technology, Massachusetts Institute of Technology, Cambridge, MA, USA. <sup>6</sup>Present address: Department of Photonics, National Yang Ming Chiao Tung University, Hsinchu, Taiwan. e-mail: [capasso@seas.harvard.edu](mailto:capasso@seas.harvard.edu); [hpahlevani@mgh.harvard.edu](mailto:hpahlevani@mgh.harvard.edu)

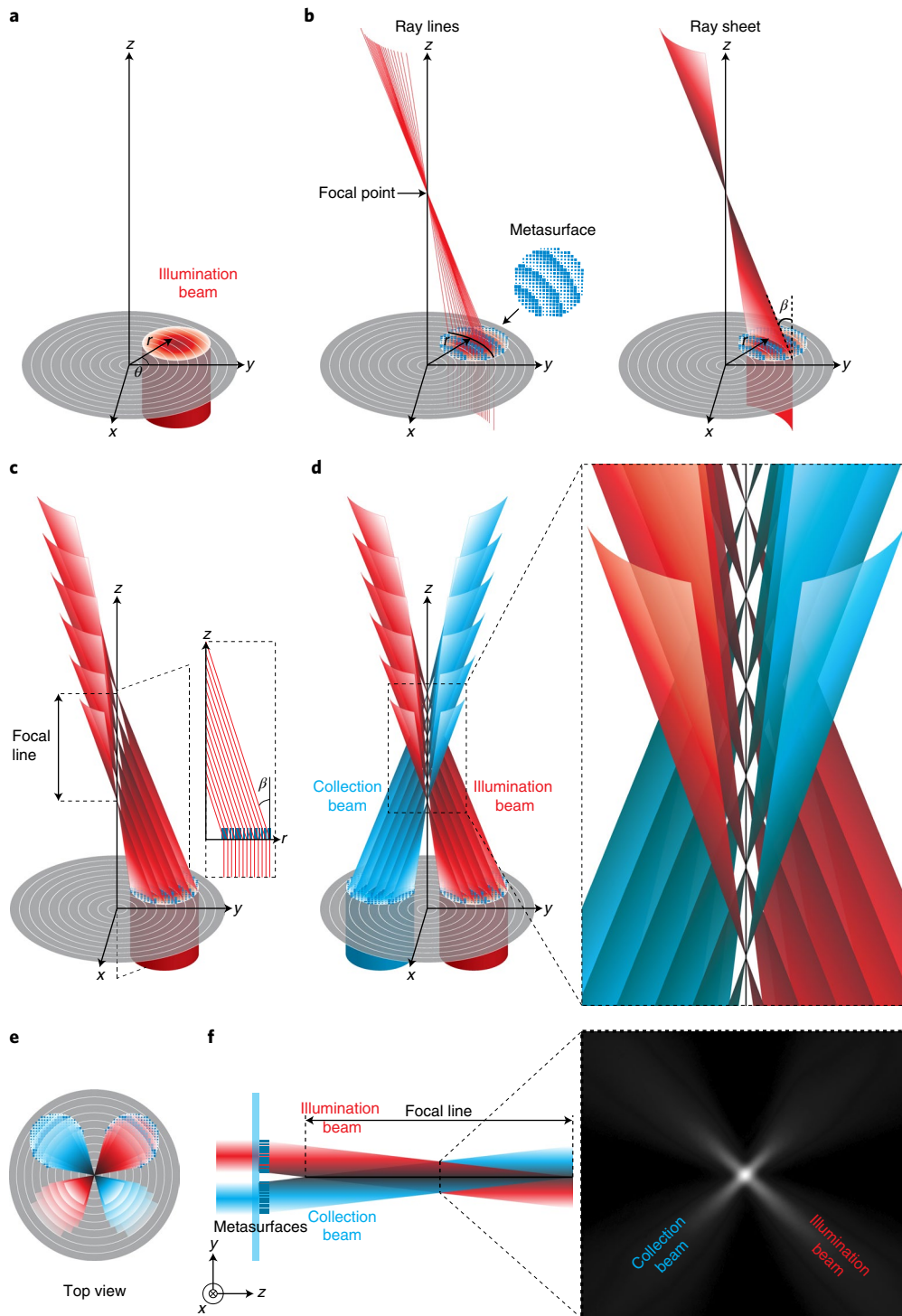


**Fig. 1 | BICI concept.** **a**, The illumination beam is generated by collimated light positioned off the imaging optical axis. **b**, The metasurface bends a ray family (sheet) originating from an arc of radius  $r$  by a constant angle  $\beta$  to form a focal point on the  $z$  axis. A family of rays originating from the same arc is shown as a ray sheet. **c**, Ray sheets subject to the same bending model constitute a focal line along the  $z$  axis. The focal line is continuous even though a finite number of focal points is illustrated for clarity. **d**, The collection metasurface establishes trajectories of collected light in ray sheets, as mirror images of illumination paths with respect to the  $x$ - $z$  plane. This configuration enables a one-to-one correspondence, that is, a bijective relation between the focal points of the illumination and collection paths, to eliminate out-of-focus signals. The magnified inset demonstrates the bijective relation. **e**, Top view of the illumination and collection beams. **f**, Schematic of the illumination and collection beams and a snapshot captured using a camera from one of the lateral planes intersecting the focal line, illustrating the actual arrangement of illumination and collection paths. This arrangement allows only the collection of photons originating from the corresponding illumination focal point.

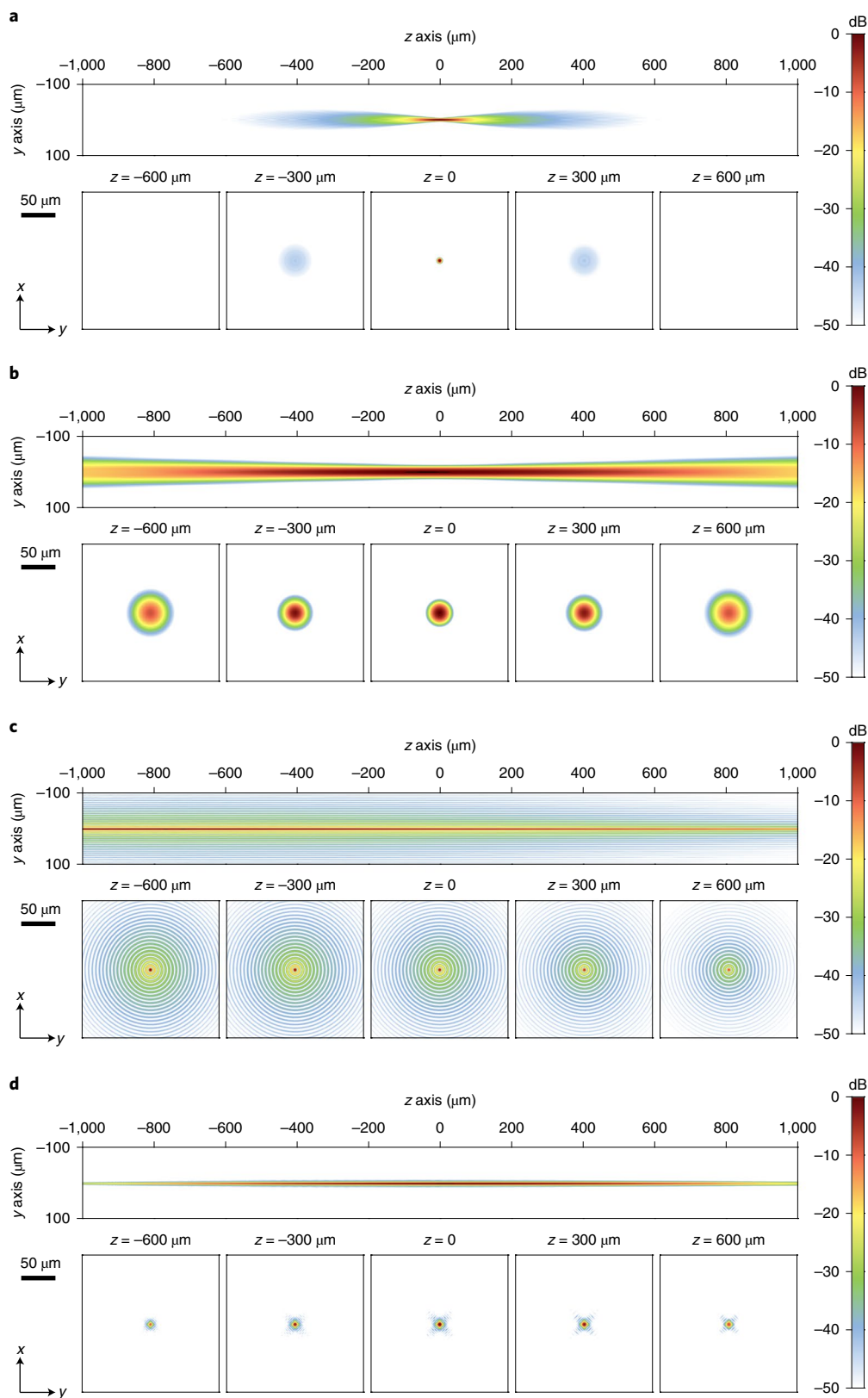


**Fig. 2 | Analytic PSF comparison of BICI with approaches using common path Gaussian and Bessel beams.** **a**, The PSF of a tightly focused Gaussian beam ( $\sim 3.2\ \mu\text{m}$  FWHM) rapidly degrades away from the focal point. **b**, The PSF of a Gaussian beam with a relatively large depth of focus ( $\sim 1.25\ \text{mm}$ ) assumes a greatly compromised lateral resolution. **c**, The PSF of a Bessel beam with a  $3.2\ \mu\text{m}$  FWHM of the central lobe involves the spread of power into several side lobes, detrimental to imaging quality. **d**, The PSF of BICI designed for a lateral resolution of  $\sim 3.2\ \mu\text{m}$  and a depth of focus of  $\sim 1.25\ \text{mm}$ . Unlike the Gaussian and Bessel beams, BICI maintains a sharp PSF over a large depth range.

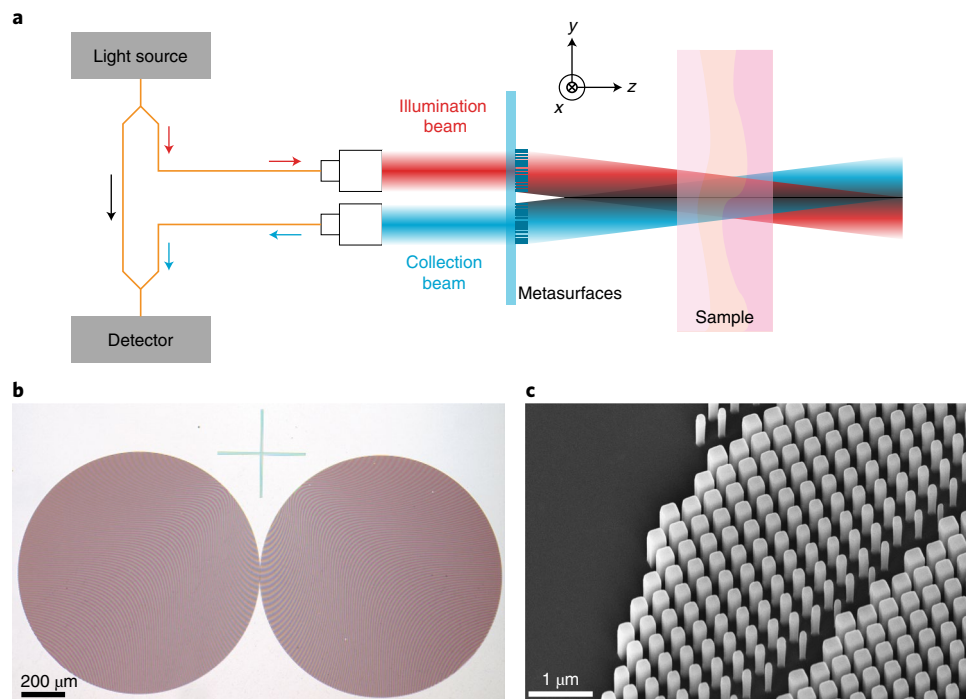


**Fig. 3 | BICI implementation.** **a**, Incorporation of BICI through one arm of an interferometer (orange lines represent a single-mode fibre). **b**, Widefield optical image of the fabricated illumination and collection metasurfaces, each 1.1 mm in diameter. The mark between the two metasurfaces coincides with the imaging optical axis. **c**, A scanning electron micrograph of the fabricated metasurface, which consists of square a-Si nanopillars.

Based on this notion, it is possible to decouple lateral resolution from the depth of focus using uniquely crafted illumination and collection paths.

In BICI, the illumination and collection paths are separated using two metasurfaces (arrays of nanoscale, subwavelength-spaced optical elements) positioned on two adjacent quadrants of a fictitious circle perpendicular to and centred at the imaging optical axis. Figure 1a,b depicts the schematics of an illumination beam impinging at a right angle on one of the metasurfaces from a collimated source. Provided that the illumination metasurface bends the ray incident on the point  $(r, \theta)$ ,  $r$  is radius and  $\theta$  is polar angle (Fig. 1a), by a constant angle  $\beta$  in the  $r$ - $z$  plane, all the rays incident on the arc of radius  $r$  will cross a single point (the focal point) on the  $z$  axis (Fig. 1b). As a result, ray families originating from arcs of constant radii on the metasurface will form a continuous focal line along the  $z$  axis (Fig. 1c). The collection metasurface (with a flipped profile of the illumination metasurface with respect to the  $x$  axis) forms ray sheets, mirror images of those in the illumination paths with respect to the  $x$ - $z$  plane (Fig. 1d,e), which are the trajectories of the collected light. A snapshot of the illumination and collection beams in one of the lateral planes intersecting the focal line is illustrated in Fig. 1f.

Remarkably, this scheme yields invariant lateral resolution (determined by  $\beta$ ) along the focal line whose length depends on the beam/metasurface size and  $\beta$ . In this configuration, illumination and collection paths overlap only on the focal points (Fig. 1f). This establishes a bijective relation defined exclusively on the focal line between the points illuminated and points from which light is collected, eliminating out-of-focus signals. This key bijective relation would be breached in the case of any overlap between the illumination and collection beams other than those on the focal line. An example of such a violation is illustrated for mispositioned illumination and collection beams in Supplementary Fig. 2.

In the existing high-resolution imaging systems, the effect of out-of-focus signals is typically lessened using tightly focused light to comparatively increase the signal from the focal point (using a

confocal geometry or non-linear effects at the focal point). This approach inevitably limits the depth range due to the severe diffraction of tightly focused light. Indispensable to high-resolution imaging, BICI rejects out-of-focus signals using the uniquely crafted illumination and collection paths without compromising the depth range.

### Design and comparison

To demonstrate the impact on imaging, we design BICI for a Fourier-domain OCT system in the near-infrared range ( $\sim 1,300 \pm 50$  nm). The bending angle  $\beta$  and the beam/metasurface size are the main parameters that govern the lateral resolution and the length of the focal line. The design procedure and justifications are described in Supplementary Section 1. Wave analyses using a Fresnel-Kirchhoff integral<sup>26</sup> were performed to engineer the imaging PSF needed for the intended resolution and depth of focus. The design parameters are selected to achieve microscopic resolution imaging in a relatively large depth range ( $>1$  mm) beyond which scattering becomes the dominant limitation. Given the design parameters (collimated beam size  $\approx 1.1$  mm;  $\beta = 21^\circ$ ), wave analyses yield a  $3.2 \mu\text{m}$  full-width at half-maximum (FWHM) of the PSF and a 1.25 mm depth of focus defined as the  $1/e^2$  PSF intensity fall-off in the axial direction.

Figure 2 presents the results of an analytic comparison of BICI with conventional approaches in terms of the lateral resolution and the depth of focus. An imaging system with a common path for illumination and collection using ideal Gaussian beams that match either the BICI lateral resolution ( $3.2 \mu\text{m}$ , Fig. 2a) or its depth of focus (1.25 mm, Fig. 2b) substantially compromises the depth of focus ( $100 \mu\text{m}$ ) or resolution ( $12 \mu\text{m}$ ), respectively. A Bessel beam with the same FWHM value of the central lobe ( $3.2 \mu\text{m}$ ), although it offers an extended depth of focus, suffers from side lobes that carry a considerable portion of optical power<sup>27,28</sup>, as illustrated in Fig. 2c. By contrast, BICI maintains a sharp PSF along a relatively large axial range (Fig. 2d) with negligible contributions from out-of-focus signals.

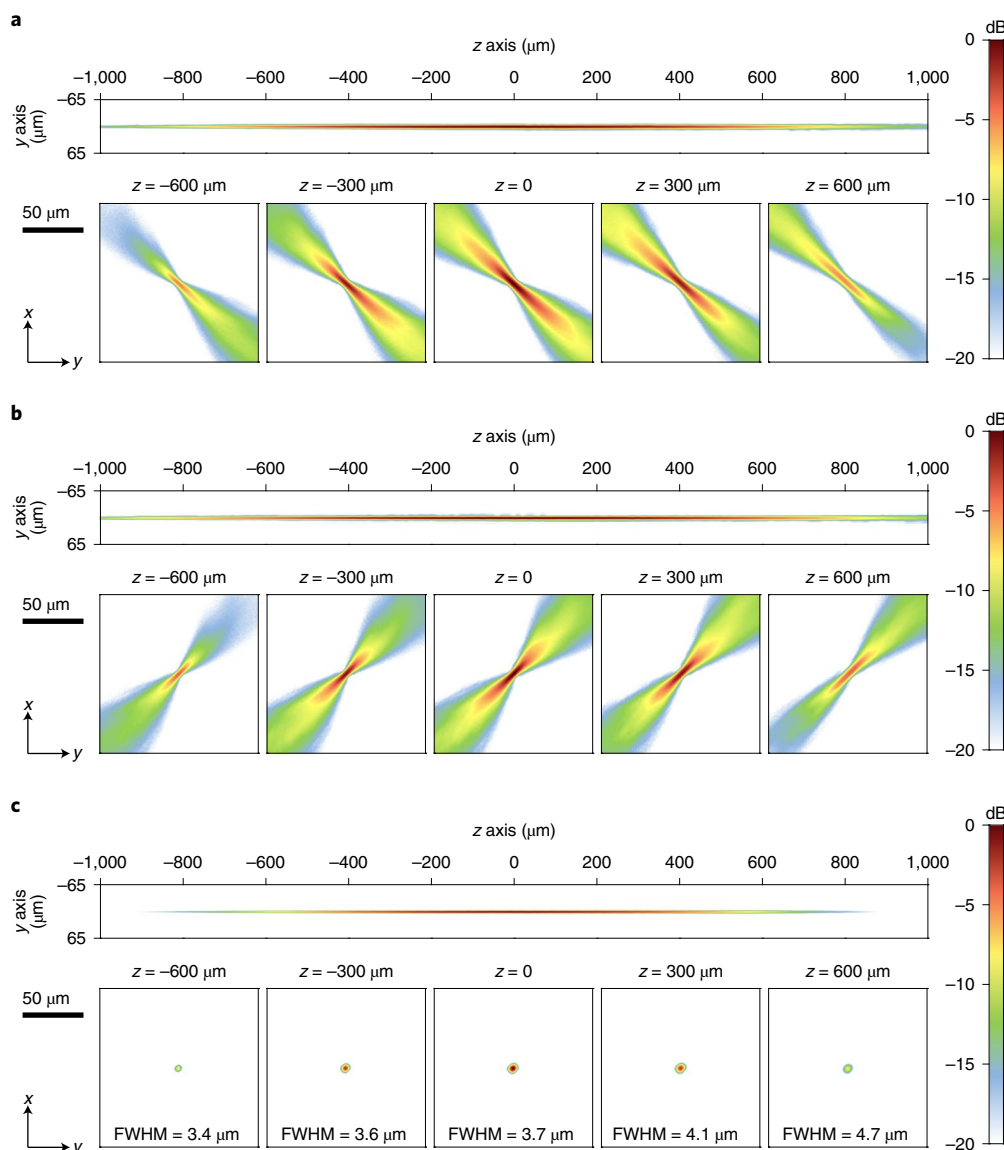


**Fig. 4 | Characterization of the BICI PSF. a, b,** Intensity distribution measurements of the illumination (**a**) and collection (**b**) beams in the  $x$ - $z$  and  $x$ - $y$  planes at 1,300 nm wavelength. The illumination and collection beams overlap only on the focal line along the  $z$  axis, demonstrating the bijective architecture. **c,** The imaging PSF, the product of the illumination and collection intensity profiles, indicates the maintenance of a sharp PSF in a large axial range. The position  $z = 0$  is -2 mm away from the metasurfaces.

### Implementation and validation

Figure 3a shows how BICI is incorporated through one arm of an interferometer. The target is axially positioned to overlap the focal line created by the metasurfaces. The distribution and geometry of the pillars on the metasurfaces are engineered to realize the illumination and collection beams in BICI. Based on the generalized Snell's law<sup>13</sup>, the phase  $\Phi$  required to bend the ray sheets (as defined in Fig. 1b) with the angle  $\beta$  in the  $r$ - $z$  plane satisfies

$$\frac{d\Phi(r)}{dr} = -\frac{2\pi}{\lambda_d} \sin(\beta) \quad (1)$$

where  $\lambda_d = 1,300$  nm is the design wavelength corresponding to the centre wavelength of the OCT source. This phase was realized by metasurfaces comprised of square amorphous silicon (a-Si) nanopillars with the same height (750 nm) distributed on a square lattice (370 nm unit cell). Nanopillars of varying base sizes across the

lattice impart the required local phase. Calculations of the cumulative phase and transmittance of the nanopillars are detailed in Supplementary Section 2. Owing to its high refractive index and low absorption in the near-infrared range<sup>29–31</sup>, a-Si is a suitable material to achieve efficient metasurfaces (>70% of the incident power concentrated on the focal line) for this application. Metasurfaces (Fig. 3b,c) were fabricated on a glass substrate using electron beam lithography (EBL)<sup>30,32</sup>. The linear phase profile in equation (1) can also be realized using an axicon. However, as detailed in Supplementary Section 1, the implementation using metasurfaces gives rise to several advantages including a superior depth of focus for a given resolution, ease of implementation and the feasibility of miniaturization for endoscopic applications.

The intensity profiles of the illumination and collection beams were measured using a custom-built optical setup (Supplementary Fig. 13). The measured illumination (Fig. 4a) and collection (Fig. 4b) beams form coincident focal lines along the  $z$  axis. Figure 4c

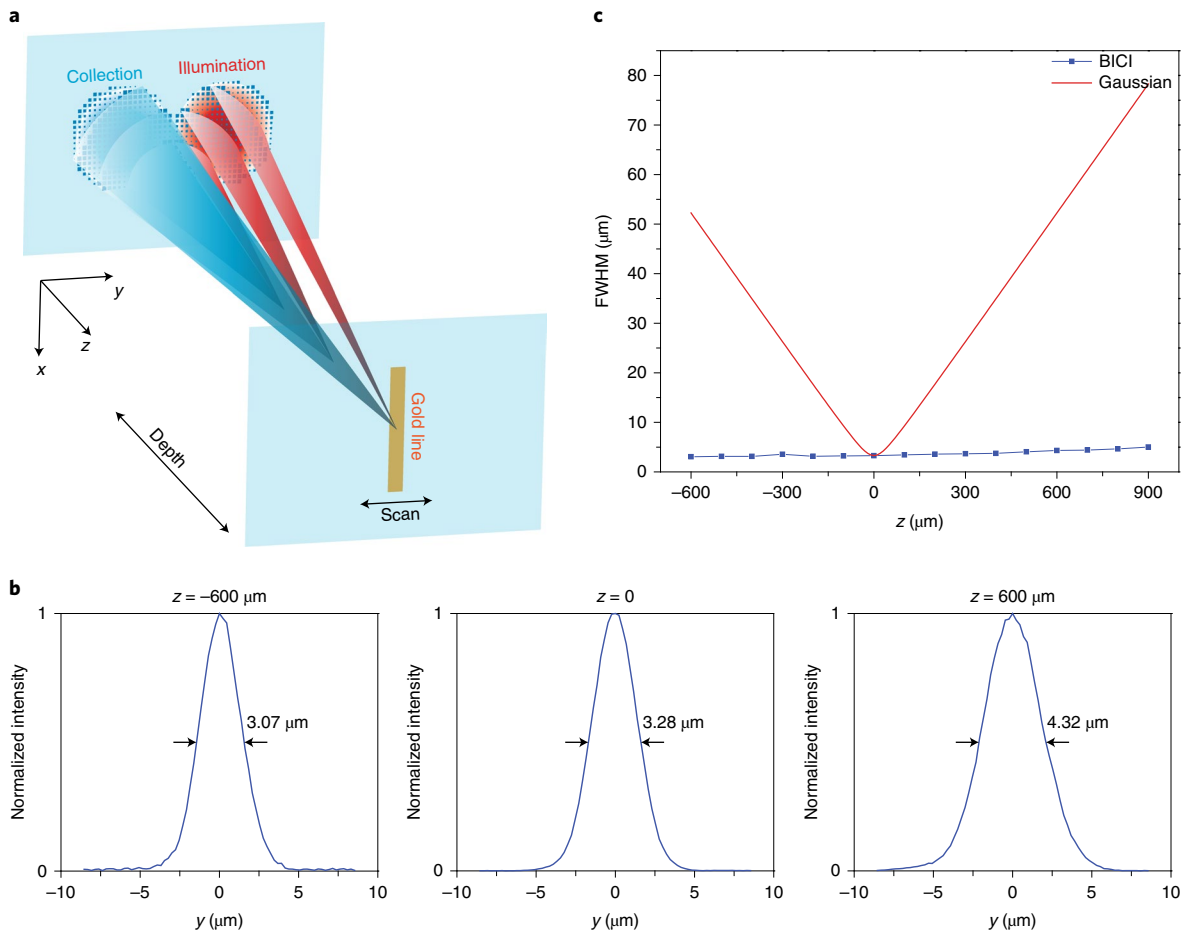


**Fig. 5 | BICI resolution and depth-of-focus measurement.** **a**, Schematic of the measurement setup for imaging a subwavelength gold line being scanned across the focal line at various depth points. **b**, Measured imaging PSF at three depth points. **c**, The measured resolution of BICI is compared with the theoretical resolution obtained from a Gaussian beam (in a common path illumination collection scheme) of the same lateral resolution, highlighting the BICI ability to maintain a high resolution in a large depth range. The position  $z=0$  is located  $\sim 2$  mm away from the metasurfaces.

indicates a sharp imaging PSF (the product of the illumination and collection intensity profiles) with small FWHM values ( $\sim 3.7 \mu\text{m}$  at  $z=0$ ) maintained over a relatively large depth range ( $\sim 1.22$  mm). These measurements are consistent with the results of wave analysis ( $3.2 \mu\text{m}$  FWHM;  $1.25$  mm depth of focus), although slight deviations exist, which are probably due to the non-linear response of the camera, alignment imperfections of the optical setup and/or fabrication errors. Despite the chromatic dispersion of the metasurfaces<sup>33–37</sup>, the focal lines of the illumination and collection beams remain aligned over the entire spectrum of the light source with negligible changes in the imaging PSF, as illustrated in Supplementary Section 1.

BICI was characterized in terms of the lateral resolution and depth of focus through the imaging of a resolution target made of a subwavelength gold line ( $200$  nm wide and  $50$  nm high) fabricated on a glass substrate. BICI was coupled to an in-house Fourier-domain OCT system<sup>38,39</sup> (Supplementary Section 4). As illustrated in Fig. 5a, the lateral resolution and depth of focus were measured by scanning the gold line across the focal line at varying target–metasurface distances. Figure 5b shows the imaging PSF measured at three selected depth points (Supplementary Fig. 16 contains the complete sets of measurements). As summarized in Fig. 5c, the results indicate a high lateral resolution ( $\sim 3.28 \mu\text{m}$ ) maintained over a depth range of more than  $1.25$  mm, which is consistent with our expectations from the wave analysis. To demonstrate the improvements, Fig. 5c also includes the analytical imaging PSF for an ideal Gaussian beam

of the same lateral resolution that demonstrates a reduced imaging depth of focus (by  $\sim 12$  times) compared with that of BICI.

There are techniques in which mathematically optimized phase profiles are imparted using freeform metasurfaces to obtain a maximum depth of focus<sup>40–43</sup>. Although these techniques can somewhat alleviate the issue through a modest increase in the depth of focus (by  $\sim 1.5$ – $2$  times), they cannot be considered as a strategy to radically overhaul the limitations in the maintenance of high-resolution imaging across a relatively large depth range.

### Imaging

We assessed the BICI capabilities to visualize tissue structures in the pulmonary airways of swine ex vivo. Freshly excised tracheo-bronchial tissue specimens were prepared and imaged using BICI and, consecutively, using a conventional approach with common illumination collection paths with a standard plano-convex lens (LA1951-C, Thorlabs). As detailed in Supplementary Section 4, this lens was chosen to match the imaging depth of focus achieved via BICI ( $\sim 1.5$  mm). Tissue specimens were laterally scanned using an automated motorized translation stage.

Figure 6 shows the images captured using BICI (Fig. 6b,d,f,h) and the conventional approach (Fig. 6a,c,e,g). A comparison indicates that BICI visualizes bronchial tissue microstructures with a superior resolving power that is preserved in a relatively large depth range. Figure 6b highlights the capability of BICI to

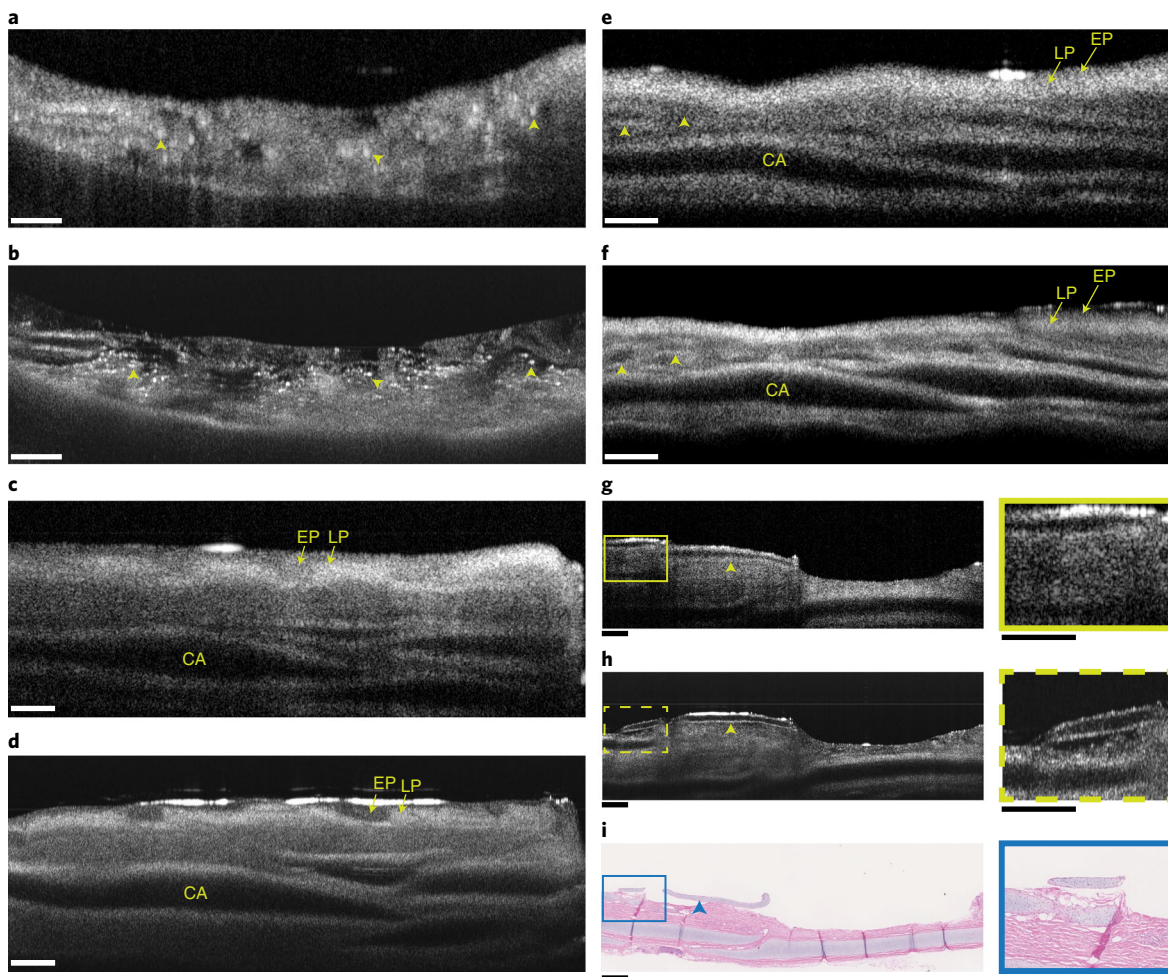


**Fig. 6 | Tissue imaging comparison of BICI and a conventional approach. a–h**, Imaging swine tracheobronchial tissue specimens using a plano-convex lens with common illumination and collection paths (**a, c, e** and **g**) and BICI (**b, d, f** and **h**). BICI provides a distinct view of the trachea tissue microstructures in **b** including inflammatory infiltrate (arrowheads), which is poorly visible in **a** captured using the conventional approach. Airway tissue layers, including the epithelium (EP), lamina propria (LP) and cartilage (CA), are clearly delineated in **d** and **f**. The arrowheads in **e** and **f** indicate glandular patterns visualized via BICI, which are not clearly discernable in the image obtained using the conventional approach. **i**, Corresponding histology image of the tissue imaged using the conventional approach (**g**) and BICI (**h**). Magnified insets are presented in solid and dashed boxes in **g–i**. BICI provides more detailed morphological information, which is closer to the structures identified in the histology image. The arrowheads in **g–i** indicate the clearly contrasted perichondrium wrapping around cartilage in the BICI image (**h**), which is poorly visible in **g**. Scale bars, 500  $\mu\text{m}$ .

distinctly visualize inflammatory infiltrate, which is poorly visible in the image captured using the conventional approach (Fig. 6a). Clear delineation of the tissue layers including the epithelium, lamina propria and cartilage deep inside the tissue are illustrated in Fig. 6d,f. This indicates that BICI provides markedly higher resolution and yet maintains a large imaging depth range nearly matching that of the conventional approach (Fig. 6c,e). Glandular patterns are also visualized via BICI in Fig. 6f, which are not clearly discernable in Fig. 6e captured using the conventional approach.

Figure 6g,h shows the results in a case where the tracheal tissue specimen underwent histological processing following optical imaging. Compared with the image obtained using the conventional approach (Fig. 6g), the image captured using BICI (Fig. 6h) carries more detailed morphological information and is closer to that provided in the histology image (Fig. 6i). As an illustration, whereas it is poorly visible in Fig. 6g, the perichondrium wrapping around the cartilage is distinctly contrasted in Fig. 6h captured using BICI.

A comparison of the images captured using BICI with those of the conventional approach indicates reduced speckles in the for-

mer. As detailed in the Discussion section, this is due mainly to the higher lateral resolution of BICI that is maintained along the depth range as well as its capability for eliminating out-of-focus and back-reflection signals.

The images shown in Fig. 6 were captured at the same illumination power ( $\sim 18$  mW) for BICI and the conventional approach. The beam arrangement in BICI results in a narrower angular range of the light collected from the points on the focal line in BICI compared with that collected using an ideal diffraction-limited lens at its focal point. This implies that the signal level at the points along the focal line in BICI is smaller than that at the focal point when imaging with an ideal diffraction-limited lens. However, this is not the case for other points along the depth range (except for the focal point) in the latter, which renders it inapt for depth imaging. As evident from the images presented in Fig. 6, this does not pose any issue in this work where BICI is applied to OCT, a highly sensitive imaging modality with a large dynamic range. In addition, the BICI capability for eliminating out-of-focus and back-reflection signals from imaging optics reduces the noise level.

## Discussion

The images presented in this work are a testament to the impact of BICI on the imaging quality. BICI entails no additional processing<sup>44</sup> or acquisition<sup>10</sup> burden and can be implemented across various wavelength ranges as its working principles remain unaltered with a wavelength change. For instance, BICI can be implemented in broadband OCT systems operating at shorter wavelengths with improved axial resolution. The wavelength range in this work is chosen to avoid the increased scattering at shorter wavelengths that predominantly limits the imaging depth<sup>10,45,46</sup>.

Various configurations of the illumination and collection beams have previously been reported in OCT (for speckle reduction<sup>47,48</sup> and deep-tissue imaging<sup>49</sup>), in two-photon microscopy (for an enhanced signal-to-background ratio<sup>50–52</sup>), in theta confocal<sup>25,53</sup>, 4Pi<sup>54</sup> and light-sheet<sup>55</sup> microscopy (for improved resolution) as well as dark-field microscopy<sup>56</sup> (for enhanced sensitivity). These systems are designed to capture signals from a region neighbouring a single focal point. As a result, imaging within a modest depth range entails either using a very small NA<sup>47–49</sup> (compromising the lateral resolution) or physical translation of the target with respect to the imaging system<sup>25,50–56</sup> (compromising the imaging speed).

Sensibly, the optical arrangement for depth imaging with preserved lateral resolution should (1) focus light equally along the depth range (on a focal line) and (2) reject out-of-focus signals that originate from the points outside the focal line. Unlike previous studies, the optical arrangement devised in BICI meets both criteria, enabling the imaging of a relatively large depth range along which the lateral resolution is maintained.

As a coherence imaging technique, OCT is comprised of speckles, which are carriers of information and, at the same time, a source of noise<sup>57</sup>. The signal-degrading speckles are due mainly to the effects of multiple backscatters, while the signal-carrying speckles are the result of the single back-scattered component whose spatial frequency content extends to the diffraction limit of the imaging optics<sup>57</sup>. Scaling up proportionally to the spot size, the signal-carrying speckles originate from the focal zone and the signal-degrading speckles are created by out-of-focus light that is scattered multiple times. It is evident from the images in Fig. 6 that, compared with the conventional approach, BICI suffers considerably less from the effects of speckles due to (1) the higher lateral resolution that is maintained along the depth range, resulting in notably smaller speckle sizes, (2) the ability to eliminate out-of-focus signals and, in turn, the effects of multiple scattering, and (3) the ability to reject back-reflection from the imaging optics.

Pathological changes in the early stages of diseases like cancer are often very subtle and can be easily overlooked. In vivo high-resolution imaging maintained in a large depth range has the potential to enable early and accurate detection and diagnosis. As it is implemented using metasurfaces, BICI can be feasibly miniaturized into endoscopic devices<sup>58,59</sup> for the in vivo high-resolution imaging of internal organs.

The advent of high-resolution optical imaging techniques has impacted fundamental medical research as well as clinical applications. Expanding the scope of applications, however, necessitates overcoming major limitations in the current techniques. The diffraction-imposed trade off between the lateral resolution and the depth of focus can be circumvented through BICI, enabling high-resolution imaging in three dimensions. Although BICI is applied to OCT in this work, the underlying concept is general and might be adapted across various imaging modalities such as confocal microscopy and two-photon microscopy.

## Online content

Any methods, additional references, Nature Research reporting summaries, source data, extended data, supplementary information, acknowledgements, peer review information; details of

author contributions and competing interests; and statements of data and code availability are available at <https://doi.org/10.1038/s41566-022-00956-6>.

Received: 1 June 2021; Accepted: 10 January 2022;

Published online: 14 February 2022

## References

- Stephens, D. J. & Allan, V. J. Light microscopy techniques for live cell imaging. *Science* **300**, 82–86 (2003).
- Denk, W., Strickler, J. H. & Webb, W. W. Two-photon laser scanning fluorescence microscopy. *Science* **248**, 73–76 (1990).
- Beaulieu, D. R., Davison, I. G., Kılıç, K., Bifano, T. G. & Mertz, J. Simultaneous multiplane imaging with reverberation two-photon microscopy. *Nat. Methods* **17**, 283–286 (2020).
- Helmchen, F. & Denk, W. Deep tissue two-photon microscopy. *Nat. Methods* **2**, 932–940 (2005).
- Huang, D. et al. Optical coherence tomography. *Science* **254**, 1178–1181 (1991).
- Fujimoto, J. G. et al. Optical biopsy and imaging using optical coherence tomography. *Nat. Med.* **1**, 970–972 (1995).
- Tearney, G. J. et al. In vivo endoscopic optical biopsy with optical coherence tomography. *Science* **276**, 2037–2039 (1997).
- Fujimoto, J. G. Optical coherence tomography for ultrahigh resolution in vivo imaging. *Nat. Biotechnol.* **21**, 1361–1367 (2003).
- Vakoc, B. J., Fukumura, D., Jain, R. K. & Bouma, B. E. Cancer imaging by optical coherence tomography: preclinical progress and clinical potential. *Nat. Rev. Cancer* **12**, 363–368 (2012).
- Zhou, K. C., Qian, R., Degan, S., Farsi, S. & Izatt, J. A. Optical coherence refraction tomography. *Nat. Photonics* **13**, 794–802 (2019).
- Curatolo, A. et al. Quantifying the influence of Bessel beams on image quality in optical coherence tomography. *Sci. Rep.* **6**, 23483 (2016).
- Zhang, M., Ren, Z. & Yu, P. Improve depth of field of optical coherence tomography using finite energy Airy beam. *Opt. Lett.* **44**, 3158–3161 (2019).
- Yu, N. et al. Light propagation with phase discontinuities: generalized laws of reflection and refraction. *Science* **334**, 333–337 (2011).
- Lin, D., Fan, P., Hasman, E. & Brongersma, M. L. Dielectric gradient metasurface optical elements. *Science* **345**, 298–302 (2014).
- Yu, N. & Capasso, F. Flat optics with designer metasurfaces. *Nat. Mater.* **13**, 139–150 (2014).
- Khorasaninejad, M. et al. Metalenses at visible wavelengths: diffraction-limited focusing and subwavelength resolution imaging. *Science* **352**, 1190–1194 (2016).
- Khorasaninejad, M. & Capasso, F. Metalenses: versatile multifunctional photonic components. *Science* **358**, eaam8100 (2017).
- Durnin, J., Miceli, J. J. & Eberly, J. H. Diffraction-free beams. *Phys. Rev. Lett.* **58**, 1499–1501 (1987).
- Berry, M. V. & Balazs, N. L. Nonspreading wave packets. *Am. J. Phys.* **47**, 264–267 (1979).
- Gutierrez-Vega, J. C., Iturbe-Castillo, M. D. & Chavez-Cerda, S. Alternative formulation for invariant optical fields: Mathieu beams. *Opt. Lett.* **25**, 1493–1495 (2000).
- Bandres, M. A., Gutierrez-Vega, J. C. & Chavez-Cerda, S. Parabolic nondiffracting optical wave fields. *Opt. Lett.* **29**, 44–46 (2004).
- Lopez-Mariscal, C., Bandres, M. A., Gutierrez-Vega, J. C. & Chavez-Cerda, S. Observation of parabolic nondiffracting optical fields. *Opt. Express* **13**, 2364–2369 (2005).
- Fahrbach, F. O., Simon, P. & Rohrbach, A. Microscopy with self-reconstructing beams. *Nat. Photonics* **4**, 780–785 (2010).
- Webb, R. H. Confocal optical microscopy. *Rep. Prog. Phys.* **59**, 427–471 (1996).
- Stelzer, E. H. K. & Steffen, L. Fundamental reduction of the observation volume in far-field light microscopy by detection orthogonal to the illumination axis: confocal theta microscopy. *Opt. Commun.* **111**, 536–547 (1994).
- Born, M. & Wolf, E. *Principles of Optics* (Pergamon, 1970).
- Blatter, C. et al. Extended focus high-speed swept source OCT with self-reconstructive illumination. *Opt. Express* **19**, 12141–12155 (2011).
- Loenser, D., Christian Singe, C., Curatolo, A. & Sampson, D. D. Energy-efficient low-Fresnel-number Bessel beams and their application in optical coherence tomography. *Opt. Lett.* **39**, 548–551 (2014).
- Fattal, D., Li, J., Peng, Z., Fiorentino, M. & Beausoleil, R. G. Flat dielectric grating reflectors with focusing abilities. *Nat. Photonics* **4**, 466–470 (2010).
- Khorasaninejad, M. & Crozier, K. B. Silicon nanofin grating as a miniature chirality-distinguishing beam-splitter. *Nat. Commun.* **5**, 5386 (2014).
- Arbabi, A., Horie, Y., Ball, A. J., Bagheri, M. & Faraon, A. Subwavelength-thick lenses with high numerical apertures and large efficiency based on high-contrast transmittarrays. *Nat. Commun.* **6**, 7069 (2015).

32. Khorasaninejad, M. & Capasso, F. Broadband multifunctional efficient meta-gratings based on dielectric waveguide phase shifters. *Nano Lett.* **15**, 6709–6715 (2015).
33. Khorasaninejad, M. et al. Achromatic metasurface lens at telecommunication wavelengths. *Nano Lett.* **15**, 5358–5362 (2015).
34. Khorasaninejad, M., Chen, W. T., Oh, J. & Capasso, F. Super-dispersive off-axis meta-lenses for compact high resolution spectroscopy. *Nano Lett.* **16**, 3732–3737 (2016).
35. Khorasaninejad, M. et al. Achromatic metalens over 60 nm bandwidth in the visible and metalens with reverse chromatic dispersion. *Nano Lett.* **17**, 1819–1824 (2017).
36. Arbabi, E., Arbabi, A., Kamali, S. M., Horie, Y. & Faraon, A. Controlling the sign of chromatic dispersion in diffractive optics with dielectric metasurfaces. *Optica* **4**, 625–632 (2017).
37. Chen, W. T. et al. A broadband achromatic metalens for focusing and imaging in the visible. *Nat. Nanotechnol.* **13**, 220–226 (2018).
38. Yun, S. H., Tearney, G. J., de Boer, J. F. & Bouma, B. E. Removing the depth-degeneracy in optical frequency domain imaging with frequency shifting. *Opt. Express* **12**, 4822–4828 (2004).
39. Yun, S. H. et al. Comprehensive volumetric optical microscopy in vivo. *Nat. Med.* **12**, 1429–1433 (2006).
40. Huang, L., Whitehead, J., Colburn, S. & Majumdar, A. Design and analysis of extended depth of focus metalenses for achromatic computational imaging. *Photonics Res.* **8**, 1613–1623 (2020).
41. Bayati, E. et al. Inverse designed metalenses with extended depth of focus. *ACS Photonics* **7**, 873–878 (2020).
42. Colburn, S. & Majumdar, A. Simultaneous achromatic and varifocal imaging with quartic metasurfaces in the visible. *ACS Photonics* **7**, 120–127 (2020).
43. Colburn, S., Zhan, A. & Majumdar, A. Metasurface optics for full-color computational imaging. *Sci. Adv.* **4**, 2114 (2018).
44. Ralston, T. S., Marks, D. L., Carney, P. S. & Boppart, S. A. Interferometric synthetic aperture microscopy. *Nat. Phys.* **3**, 129–134 (2007).
45. Liu, L. et al. Imaging the subcellular structure of human coronary atherosclerosis using micro-optical coherence tomography. *Nat. Med.* **17**, 1010–1014 (2011).
46. Yuan, W., Brown, R., Mitzner, W., Yarmus, L. & Li, X. Super-achromatic monolithic microprobe for ultrahigh-resolution endoscopic optical coherence tomography at 800 nm. *Nat. Commun.* **8**, 1531 (2017).
47. Desjardins, A. E. et al. Angle-resolved optical coherence tomography with sequential angular selectivity for speckle reduction. *Opt. Express* **15**, 6200–6209 (2007).
48. Klein, T., Raphael, A., Wolfgang, W., Tom, P. & Huber, R. Joint aperture detection for speckle reduction and increased collection efficiency in ophthalmic MHz OCT. *Biomed. Opt. Express* **4**, 619–634 (2013).
49. Zhao, Y. et al. Dual-axis optical coherence tomography for deep tissue imaging. *Opt. Lett.* **42**, 2302–2305 (2017).
50. Cheng, X. et al. Comparing the fundamental imaging depth limit of two-photon, three-photon, and non-degenerate two-photon microscopy. *Opt. Lett.* **45**, 2934–2937 (2020).
51. Wang, C., Qiao, L., Mao, Z., Cheng, Y. & Xu, Z. Reduced deep-tissue image degradation in three-dimensional multiphoton microscopy with concentric two-color two-photon fluorescence excitation. *J. Opt. Soc. Am. B* **25**, 976–982 (2008).
52. Kobat, D., Zhu, G. & Xu, C. Background reduction with two-color two-beam multiphoton excitation. In *Proc. Biomedical Optics* paper BMF6 (Optical Society of America, 2008); <https://doi.org/10.1364/biomed.2008.bmf6>
53. Liu, J. T. C. et al. Dual-axes confocal reflectance microscope for distinguishing colonic neoplasia. *J. Biomed. Opt.* **11**, 054019 (2006).
54. Hell, S. & Stelzer, E. H. K. Properties of a 4Pi confocal fluorescence microscope. *J. Opt. Soc. Am. A* **9**, 2159–2166 (1992).
55. Power, R. M. & Huisken, J. A guide to light-sheet fluorescence microscopy for multiscale imaging. *Nat. Methods* **14**, 360–373 (2017).
56. Gao, P. F., Lei, G. & Huang, C. Z. Dark-field microscopy: recent advances in accurate analysis and emerging applications. *Anal. Chem.* **93**, 4707–4726 (2021).
57. Schmitt, J. M., Xiang, S. H. & Yung, K. M. Speckle in optical coherence tomography. *J. Biomed. Opt.* **4**, 95–105 (1999).
58. Pahlevaninezhad, H. et al. Nano-optic endoscope for high-resolution optical coherence tomography in vivo. *Nat. Photonics* **12**, 540–547 (2018).
59. Gissibl, T., Thiele, S., Herkommer, A. & Giessen, H. Two-photon direct laser writing of ultracompact multi-lens objectives. *Nat. Photonics* **10**, 554–560 (2016).

**Publisher's note** Springer Nature remains neutral with regard to jurisdictional claims in published maps and institutional affiliations.

© The Author(s), under exclusive licence to Springer Nature Limited 2022

## Methods

**Fabrication process.** The metasurfaces were fabricated using a top-down lithography technique<sup>30,32</sup>. A 750-nm-thick a-Si layer was deposited on a glass substrate using plasma-enhanced chemical vapour deposition. EBL was used to create the intended pattern on a negative-tone photoresist (ma-N 2403, micro resist technology). Deep reactive ion etching was then used to generate the a-Si nanopillars.

The resolution target was also fabricated via the EBL of a line pattern on a positive-tone photoresist (ZEP520A, Zeon Chemicals), followed by the deposition of a gold layer of 50 nm thickness using thermal evaporation and a lift-off process.

## Data availability

All data generated and analysed are included in the paper and its supplementary information. The imaging data presented in Fig. 6 are available at [https://figshare.com/articles/figure/Fig\\_6e\\_TIF/17124062](https://figshare.com/articles/figure/Fig_6e_TIF/17124062).

## Code availability

All custom codes or algorithms used to generate results that are reported in this manuscript are available from the corresponding authors upon reasonable request.

## Acknowledgements

This project was supported by funding from the Department of Defense under grant no. W81XWH2010300 awarded to H.P., the Natural Sciences and Engineering Research Council of Canada under grant no. 392075 awarded to M. Pahlevani and the National Institutes of Health under grant no. 5R01HL133664 and grant no. 1R01CA255326 awarded to M.J.S. This work was performed in part at Harvard's Center for Nanoscale

Systems (CNS), a member of the National Nanotechnology Coordinated Infrastructure (NNCI), supported by the National Science Foundation (NSF) under NSF award no. 1541959.

## Author contributions

M. Pahlevaninezhad and H.P. conceived the design and implementation and executed the experiments. M. Pahlevani, M.J.S., B.B. and F.C. refined the methodology. M. Pahlevaninezhad performed computational analyses for metasurface design. M. Pahlevaninezhad and Y.-W.H. fabricated the metasurfaces. H.P., M. Pahlevaninezhad and M.J.S. performed ex vivo imaging and processed the imaging data. M. Pahlevaninezhad and H.P. prepared the original manuscript with contributions from F.C., M. Pahlevani, B.B. and M.J.S. The research was supervised by H.P. and F.C.

## Competing interests

The authors declare no competing interests.

## Additional information

**Supplementary information** The online version contains supplementary material available at <https://doi.org/10.1038/s41566-022-00956-6>.

**Correspondence and requests for materials** should be addressed to Federico Capasso or Hamid Pahlevaninezhad.

**Peer review information** *Nature Photonics* thanks the anonymous reviewers for their contribution to the peer review of this work.

**Reprints and permissions information** is available at [www.nature.com/reprints](http://www.nature.com/reprints).